

Article

Finite Element Modeling and Stress Analysis of a Six-Splitting Mid-Phase Jumper

Pengfei Ma ¹, Yongjie Li ², Jiceng Han ³, Cheng He ² and Wenkai Xiao ^{1,*}¹ Power & Mech Engn, Wuhan University, Wuhan 430072, China; mpf01234@163.com² Electric Power Research Institute, State Grid Xinjiang Electric Power Company Limited, Xinjiang 830000, China; 13909972277@139.com (Y.L.); xjdkyh@163.com (C.H.)³ Electric Power Research Institute, State Grid Fujian Electric Power Company Limited, Fujian 350000, China; hanjiceng1989@163.com

* Correspondence: xiaowenkai@whu.edu.cn

Received: 29 November 2019; Accepted: 13 January 2020; Published: 16 January 2020



Abstract: In this study, a finite element, fully three-dimensional solid modeling method was used to study the mechanical response of a steel-cored aluminum strand (ACSR) with a mid-phase jumper under wind load. A whole model (simplifying an ACSR into a solid cylinder) and a local model (modeling according to the actual structure of an ACSR) of the mid-phase jumper were established. First, the movement of the mid-phase jumper of the tension tower under wind load was studied based on the whole finite element model, and the equivalent Young's modulus of the whole model was adjusted based on the local model. The results of the whole model were then imported into the local model and the stress distribution of each strand of the ACSR was analyzed in detail to provide guidance for the treatment measures. Therefore, the whole model and the local model complemented each other, which could reduce the number of model operations and ensure the accuracy of the results. Through the follow-up test to verify the results of the finite element simulation and the comparison of the simulation and fatigue test results, the causes of the broken strand of the ACSR were discussed. Although this modeling method was applied to the stress and deformation analysis of a mid-phase jumper in this study, it can be used to study the bending deformation of rope structures with a complex geometry and the main bending deformation. In addition, the effect of the friction coefficient on the bending of the mid-phase jumper was studied.

Keywords: finite element modeling; aluminum conductor steel-reinforced cable; bend deformation; stress; friction coefficient; wind loads; fatigue fracture

1. Introduction

Fatigue of the wires in an overhead conductor occurs within the couplings that restrict the conductor vibration from incurring a vortex-induced oscillation [1–3]. At present, most of the overhead conductors are made of steel-cored aluminum strands (ACSRs), and ACSR is widely used in power delivery systems around the world [4,5]. An aeolian vibration is one of the causes of a fretting fatigue failure of a conductor. Such failures invariably occur in suspension clamps, dampers, and spacers [6,7].

The northwest part of China has several areas with a strong wind, which significantly impacts the operation of transmission and transformation lines. According to statistics, from July 2015 to September 2016, 750 kV ultra-high voltage (UHV) transmission lines undertaking the task of power transmission from the west to the east in a strong wind areas suffered three strand breaks of the mid-phase jumper in succession, resulting in significant economic losses. Therefore, it is very important to study the stress and deformation distribution of the mid-phase jumper in terms of the movement under strong winds to provide guidance for the treatment measures.

Rizzo et al. [8] described a method based on outlier analysis and the wavelet transform for structural damage detection based on guided ultrasonic waves. Furthermore, this method was applied to the detection of notch-like defects in a seven-wire strand by using built-in magnetostrictive devices for ultrasound transduction. Castellano et al. [9] presented an innovative non-destructive experimental technique based on ultrasonic waves for a quantitative determination of the damage level in structural components. Neslušan et al. [10] presented a systematic study using a magnetic non-destructive evaluation of corrosion attack in rope wires via Barkhausen noise emission. Because of the complexity of the scene, it is difficult to detect the damage of a six-splitting mid-phase jumper directly. Through the establishment of the finite element model six-splitting of a mid-phase jumper, the damage under wind load can be calculated. This paper presents an effective finite element modeling method for a large steel-cored aluminum strand when a main bending deformation occurs.

Because of the interaction between strands, multi-layer strands have a variable bending stiffness. With the bending of the strands, they begin to gradually slide with respect to each other, resulting in a decrease in the bending stiffness. However, the structural model of the conductor studied here is larger and has a spatial bending form. Therefore, it is extremely difficult to establish a finite element model of a mid-phase jumper with equal proportions.

Some scholars have proposed different modeling methods to study the mechanical response of steel strands during a bending deformation. Raouf and Hobbs [11] idealized a strand as a series of concentric orthotropic cylinders, each of which is associated with a specific layer and its corresponding mechanical properties. The bending process of the wire was also considered. In addition, Lanteigne [12] studied the mechanical behavior of cables under an arbitrary combination of tension, torsion, and bending. The force model of the cables is universal.

Leclair and Costello [13] applied the love crank balance equation to each conductor and deduced a mechanical conductor model that can predict the stress of single twisted strands under axial, bending, and torsion loads. Hong et al. [14] established a mechanical model of the conductor bending behavior under tension, although the model was significantly simplified. For example, the contact between adjacent cables of the same layer is neglected in the established model, and the contact line is used instead of the contact point of the superimposed layer. In addition, the cross-section of the twisted strand after bending is still planar.

Judge et al. [15] used LS-DYNA to establish a full three-dimensional, elastic–plastic finite element model of multi-layer helical cables under a quasi-static axial load. The model uses three-dimensional solid elements to discretize each strand and simulates the contact types between all strands. The model also uses the law of non-linear hardening to explain the plastic deformation. Zhang et al. [16] succeeded in analyzing the flexural stiffness of the strands using a solid three-dimensional finite element model, although their research was limited to single-pitch, single-layer cables. To summarize, the method of full three-dimensional solid modeling considers the contact between wires, among other factors, which results in a large number of computations, and thus the length of a fully three-dimensional solid element finite element model is usually very short. To reduce the computational complexity of the model, some scholars have used a beam element instead of solid element to establish a finite element model of a strand. Zhou et al. [17] used a beam element to model a single-layer conductor and managed the contact interaction between the lines using a coupling equation between the corresponding nodes, and thus the slip between the lines was not considered. The model was applied to the analysis of strands under bending loads, which is still limited to single-layer strands with a small deflection. Beleznai et al. [18] also modeled a conductor. Each line contact was simulated using a spring element. The stiffness of the spring element was based on the Hertzian contact theory. Although the correctness of this method has been proved, its application was still limited to single or double layers with a small displacement. Lalonde et al. [19,20] proposed a finite element modeling method for multi-layer steel strands under multi-axial loads. This method utilizes a beam element and a three-dimensional line contact, which greatly reduce the computational complexity of the model under the premise of ensuring a high level of accuracy.

In this study, a finite element, fully three-dimensional solid modeling method was used to study the mechanical response of a steel-cored aluminum strand with a mid-phase jumper under a bending deformation. A whole model (simplifying an ACSR into a solid cylinder) and a local model (modeling according to the actual structure of an ACSR) of the mid-phase jumper were established. First, the movement of the mid-phase jumper of the tension tower under wind load was studied based on the whole finite element model, and the equivalent Young's modulus of the whole model was adjusted based on the local model. The results of the whole model were then imported into the local model, and the stress distribution of each strand of the ACSR was analyzed in detail under a bending deformation to provide guidance for the treatment measures. Therefore, the whole model and the local model complemented each other, which could reduce the number of model operations and ensure the accuracy of the results. The feasibility of this method was verified through a comparison with the results of subsequent experiments. Although this modeling method was applied to the stress and deformation analysis of a mid-phase jumper in this study, it can be used to study the bending deformation of rope structures with a complex geometry and the main bending deformation. The finite element modeling method of a mid-phase jumper presented in this paper can be implemented in any general finite element software. Abaqus (2018, Dassault Systemes Simulia Corp, Johnston, RI, USA) was also used in this study.

2. Finite Element Modeling Approach

2.1. Spatial Structure and Motion Form of the Mid-Phase Jumper

Figure 1a shows the location of a mid-phase jumper on a tension tower and Figure 1b shows the lateral view of a mid-phase jumper on a tension tower. Because of the tension at both ends of the tower, large-span wires are subjected to a significant amount of tension. However, for a mid-phase jumper, owing to its different spatial structure, the force differs from that of a large-span wire. As shown in Figure 1a, b, the lower end of the mid-phase jumper is fixed by a tension clamp and the upper end is suspended by an insulator string, which shows a spatial tortuous distribution. Compared with a large-span wire, the initial tension applied to the mid-phase jumper is very small, and thus the initial tension applied to the mid-phase jumper can be neglected. Figure 1c shows an image of the motion of the lower end of a mid-phase jumper near a fixed position under level-7 wind. It is seen that the mid-phase jumper oscillates along the A-B direction under a strong wind, and its range of motion is slightly larger than the diameter of the six-splitting spacer (650 mm). In addition, the oscillation frequency is 5–8 times per minute. As shown in Figure 1d, the broken position of the mid-phase jumper is at the outlet of the tension clamp. The common motion forms of an overhead conductor under wind load are breeze vibration, subspan vibration, galloping, etc. [21–23]. The frequency of aeolian vibration is generally 3–150 Hz, and the amplitude is $0.01-1d$ (d is the diameter of the conductor), which occurs when the wind speed is small. The frequency of galloping is 0.08–3 Hz, and the amplitude is much larger than that of aeolian vibration, which often occurs on the iced conductor with a high wind speed. Subspan oscillation refers to the vibration of a conductor between adjacent spacer bars under wind load. The amplitude of subspan oscillation is generally 5–10 mm and the frequency of oscillation is 1–2 Hz. To sum up, the movement form of the mid-phase jumper is different from the breeze vibration, the subspan vibration, and the galloping, which is a large-scale cyclic swing under a strong wind.

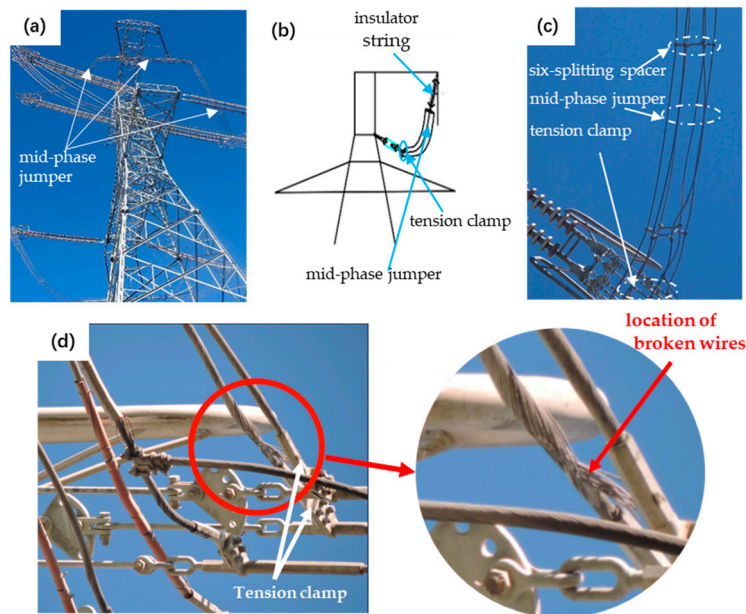


Figure 1. (a) Position of a mid-phase jumper on a tension tower, (b) lateral view of a mid-phase jumper on a tension tower, (c) movement of a mid-phase jumper near a tensile clamp, and (d) position of broken strands on the site of a mid-phase jumper.

2.2. Establishment of the Whole Model

Figure 2a shows the structure of the mid-phase jumper and the related data size (mm). It is seen that the mid-phase jumper includes a six-splitting, steel-cored aluminum strand and a six-splitting spacer. Figure 2b shows a side view of a mid-phase jumper on a tension tower. Figure 2c shows the solid model of the mid-phase jumper imported into Abaqus, which simplified the steel-core aluminum wire into a solid rod and was established in SolidWorks. (2016, Dassault Systemes Simulia Corp, Johnston, RI, USA) Because the lower end of the mid-phase jumper was rigidly connected through a tension clamp, all degrees of freedom of the lower end of the mid-phase jumper were fixed. As shown with the A arrows, the fixed ends of the lower of the mid-phase jumper were the outlet position of the tension clamp. In the actual structure of the mid-phase jumper, the top of the insulator string was fixed on the tension tower. According to the assembly of the insulator string and the mid-phase jumper, the maximum displacement of the middle section of the mid-phase jumper deviating from the east–west direction was limited to 30 mm, and other displacement degrees of freedom and all rotational degrees of freedom were limited, as shown with the B arrows. Because of the large deformation of the mid-phase jumper under a strong wind, geometric nonlinearity was opened during the analysis step of Abaqus. The quadratic tetrahedron stress element (C3D10) with a high accuracy was used in the whole model. The number of elements and nodes were approximately 3.5×10^5 and 6.6×10^5 , respectively.

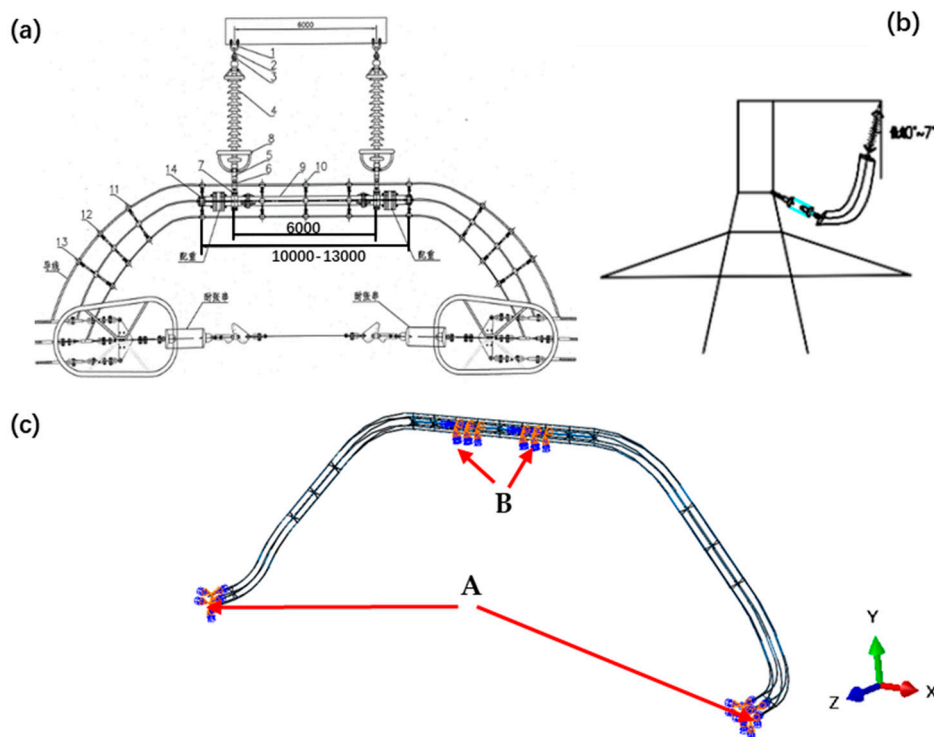


Figure 2. (a) Structural diagram of a mid-phase jumper, (b) side view of a mid-phase jumper on a tower, and (c) finite element model of a mid-phase jumper in Abaqus.

2.3. Establishment of Local Model

As shown in Figure 1d, the actual fracture position of the mid-phase jumper is the outlet position of the tension clamp. In order to accurately analyze the stress distribution of the actual fracture position, a local model was established. The local model established in this study consisted of four helical layers wound around a straight cylinder at the center. In addition, adjacent spiral layers were wound in the opposite directions to reduce the internal torque caused by the winding. The formula for calculating the radius of each helical layer is shown in Equation (1). The formula for calculating the helix angle is shown in Equation (2). In Equations (1) and (2), R_i , d_i , d_{core} , m_i , and a_i indicate the layer radius (mm), wire diameter (mm), diameter of the central steel wire (mm), pitch diameter ratio, and helical angles of the helical layers, respectively.

$$R_i = \frac{d_{core}}{2} + \frac{d_i}{2} + \sum_{k=1}^{k=i-1} d_k \tag{1}$$

$$a_i = \arctan\left(\frac{m_i}{\pi}\right) \tag{2}$$

Table 1 shows the mechanical properties of the materials and modeling parameters of the local finite element model. Figure 3a shows the sectional diagram of the local finite element model. As shown in Figure 3b, a section of all strands was fixed at one end of the local model. The fixed end was located at the outlet of the tension clamp. By setting the motion coupling constraints in Abaqus, the other end was coupled with the central point, all six degrees of freedom of the constrained area were selected to be coupled with the coupling points, and the constrained end face then became a rigid plane. There was no relative displacement between the nodes in the constrained area, only a rigid motion with the selected coupling point. In this case, the displacement boundary condition (Y_a) could be applied to the coupling point.

Table 1. Mechanical properties of materials and modeling parameters of the local finite element model.

Line Strand of Position	Number of Strands	E (GPa)	Yield Strength (MPa)	Poisson Ratio	Winding Angle (°)	Pitch Ratio	Diameter (mm)
Outermost layer	24	69	275	0.30	74.0	11	3.07
Layer 3	18	69	275	0.30	75.3	12	3.07
Layer 2	12	69	275	0.30	76.4	13	3.07
Layer 1	6	207	68	0.28	81.5	21	3.07
Central steel wire	1	207	68	0.28	0	—	3.07

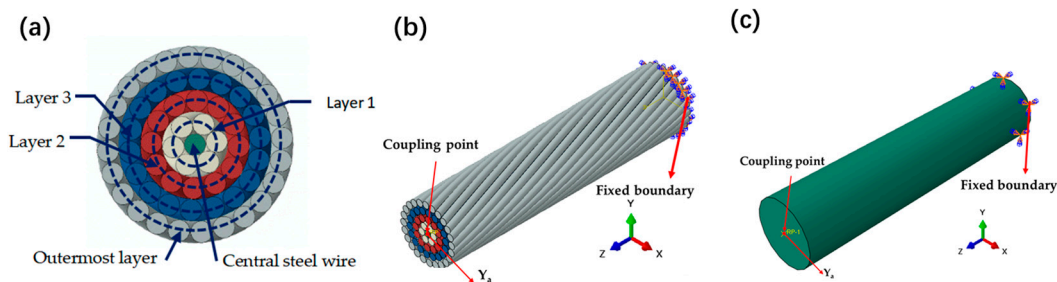


Figure 3. (a) Sectional diagram of the local finite element model, (b) 3-D local finite element model, and (c) the whole microsegment finite element model.

The hexahedral incompatible element (C3D8I) was used in the local model. The number of elements and nodes were approximately 1.3×10^5 and 1.8×10^5 , respectively. The default contact behavior in the Abaqus/Standard was the “hard contact.” The surface contact was set between each strand. Although numerous contact algorithms can be used to establish contact pairs, the contact is extremely complex owing to the large number of surface-to-surface contacts involved. Therefore, the contact algorithm was set as the augmented Lagrange algorithm, which improved the convergence efficiency of the model operation under the premise of ensuring the accuracy. The default value of the contact stiffness was adopted, and the expansion coefficient of the contact stiffness was 1.

Although Utting and Jones [24] explored the friction effect between steel wires, they were not specified regarding the friction coefficient. Judge et al. [15] and Lalonde et al. [19] applied a friction coefficient μ of 0.115 to all contact points. The present simulation used the same coefficient value. When the mid-phase jumper sways significantly under wind load, the main deformation of the mid-phase jumper is bending. Therefore, the bending stiffness of the whole model was made the same as that of the local model by adjusting the Young’s modulus parameters, and the adjusted Young’s modulus was then input into the whole model for the calculations. Finally, the motion behavior of the whole model under wind load was obtained. The adjustment process of the Young’s modulus of the whole model is described in detail in Section 3.

2.4. Application of Wind Load on the Whole Model

A mid-phase jumper oscillates under wind load. According to Bernoulli’s equation, the wind load on the conductor is as shown in Equation (3):

$$P = \frac{\gamma}{2g} v^2 \sin \theta. \tag{3}$$

In Equation (3), P , γ , g , v , and θ indicate the wind load (N), the air density (kg/m^3), acceleration of gravity (m/s^2), wind speed (m/s), and angle between the wind direction and conductor axis, respectively. For a large-span conductor, an aerodynamic coefficient and a nonuniformity coefficient were introduced. According to Equation (3), the main factors influencing the wind load on the conductor are the wind

speed and angle θ between the wind direction and conductor. When θ is 90° , the formula for calculating the wind load is shown in Equation (4):

$$P_f = a_f \cdot K_a \cdot A_f \cdot \frac{v_f^2}{1600}, \tag{4}$$

In Equation (4), a_f indicates the asymmetrical coefficient of the wind pressure. When the wind speed is less than 20 m/s, a_f is taken to be 1, and when the wind speed is between 20 and 30 m/s, it is taken to be 0.85. In addition, K_a indicates the aerodynamic coefficient and is taken to be 1, A_f represents the projected area of the conductor in the direction of the wind load, and v_f indicates the speed (m/s). Finally, P_f indicates the wind load (N). The amplitude change of the wind load applied on the mid-phase jumper is shown in Equation (5):

$$A_{mp} = \sin\left(\frac{\pi}{2}t\right) \tag{5}$$

In Equation (5), A_{mp} indicates the amplitude of wind load applied, and t indicates the time (s). The wind load is converted from the kinetic energy of the wind, and the kinetic energy consumption of the wind perpendicular to the conductor is the largest; therefore, the wind speed component perpendicular to the strand determines the actual wind load, and that parallel to the conductor has little effect. Table 2 shows the applied wind speed level to the whole model, the corresponding wind speed, and the magnitude of the applied wind load when θ was 90° . Westerly winds dominate the northwest part of China throughout the year. In this study, the mechanical response of the mid-phase jumper to a westerly wind was mainly considered. As shown in Figure 4, the wind load was applied to the whole model, and the arrow in the figure represents the wind load and wind direction.

Table 2. Magnitude of wind load applied to the surface of the conductor corresponding to different wind speeds.

Wind Speed Level	Wind Speed (m/s)	Wind Load (MPa)
1	1.0	2.39×10^{-7}
2	2.0	1.49×10^{-6}
3	3.5	4.83×10^{-6}
4	5.5	1.01×10^{-5}
5	8.0	2.15×10^{-5}
6	11.0	2.41×10^{-5}
7	14.0	3.90×10^{-5}

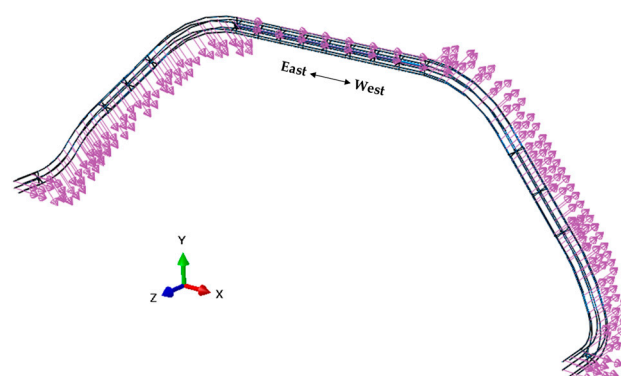


Figure 4. Wind load applied to the whole model.

2.5. Model Solution

The whole model used the Newton–Raphson algorithm to solve non-linear problems with a large displacement. The local model used the Newton–Raphson method to solve the contact and material nonlinearity problems. All simulations conducted in this study were implemented on a 2.3 GHz, 24-core CPU and a computer with 64 GB of memory.

3. Matching Adjustment of Whole Model and Local Model

On the one hand, in order to accurately simulate the deformation of a six-splitting mid-phase jumper under wind load, it is necessary to adjust the equivalent Young's modulus of the whole model to make it have the same bending resistance as the local model. On the other hand, in order to more accurately simulate the stress of each strand of a conductor at the outlet of the tension clamp, it is necessary to ensure the accuracy of the deformation of the whole model introduced into the local model, that is, to ensure that the whole model has the same bending resistance as the local model. Therefore, it is very important for the accuracy of the simulation results to adjust the Young's modulus of the whole model and obtain the equivalent Young's modulus of the whole model based on the local model.

The Young's modulus of the whole model is really the key of this paper, which was determined using the following method. In order to determine the Young's modulus of the whole model, as shown in Figure 3c, the whole microsegment model with a length of 120 mm was established, which was consistent with the cross section of the whole model (27.63 mm). By adjusting the Young's modulus of the whole microsegment model, the whole microsegment model and the local model had the same bending stiffness, and then the adjusted Young's modulus was input into the whole model such that the whole model had the same bending stiffness as the local model. A hexahedral incompatible element (C3D8I) was used in the whole microsegment model. The number of elements and nodes were approximately 2.4×10^4 and 2.6×10^4 , respectively. One end of the whole microsegment model was completely fixed, while the other end was coupled with the central point, and the displacement boundary condition (Y_a) was applied to the coupling point. The boundary conditions of the microsegment whole model were in good agreement with those of the local model.

The Y_a of the coupling point and the force (F) needed to achieve the Y_a were obtained by changing Y_a . As shown in Figure 5a, for the local model, the relationship of $F - Y_a$ was approximately linear. By continuously adjusting the Young's modulus of the whole microsegment model, the relationship of $F - Y_a$ under different Young's moduli can be obtained, and the relationship of $F - Y_a$ was approximately linear. As shown in Figure 5a, when the Young's modulus of the whole microsegment model was 6.25 GPa, the $F - Y_a$ lines of the whole microsegment model and the local model almost coincided. Therefore, when the Young's modulus of the whole microsegment model was 6.25 GPa, the whole microsegment model and the local model had a similar bending stiffness. Then, 6.25 GPa was input into the whole model, which had the same bending stiffness as the local model.

As shown in Figure 5b, for the same Y_a , the difference in F between the whole microsegment model and the local model was defined as ΔF . Based on an F corresponding to a Y_a of the local model, the ratio of ΔF to F corresponding to Y_a of this model was the error when applying this method. As shown in Figure 5b, Y_a had a larger error of 0–0.25 mm and a smaller error of 0.25–0.6 mm. According to the simulation results in the fourth section, Y_a corresponding to a strong wind was between 0.25–0.60; therefore, this study mainly considered the part of Y_a between 0.25 and 0.60 mm. The absolute error of this part was less than 10%, which is within a reasonable range.

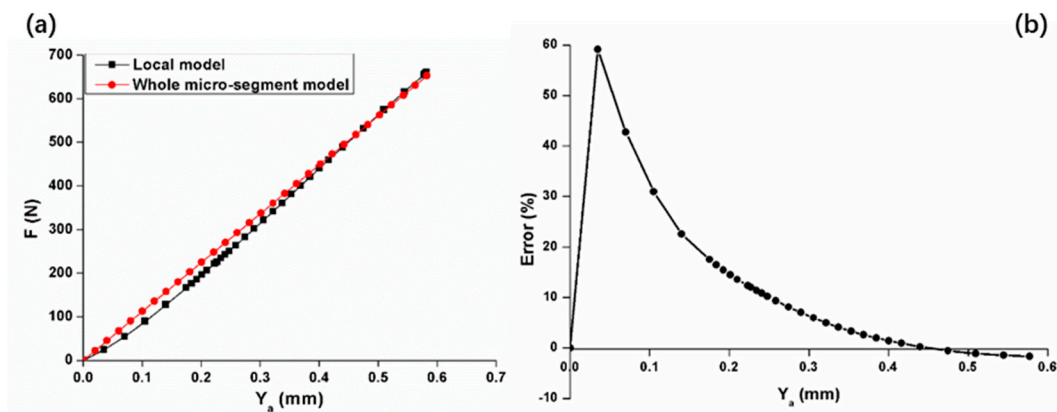


Figure 5. (a) $F - Y_a$ of the whole microsegment model and the local model, and (b) the error of the whole model.

4. Results and Discussion

Figure 6a shows a displacement nephogram of the whole model under a westerly, level-6 wind. Figure 6b shows the displacement nephogram of the whole model with a length of 1000 mm at the outlet of the tension clamp. The middle section of the mid-phase jumper swung back and forth along the east–west direction. The swing of the mid-phase jumper in this direction caused a greater bending moment at the lower area of the mid-phase jumper.

It was assumed that the deflection of the conductor with the maximum displacement at the lower area of the whole model under wind load was Y_b at 89 mm away from the outlet of the tension clamp. When Y_b corresponding to different wind loads was imported into the local model, the maximum equivalent stress (σ_a) corresponding to the outlet position of the tension clamp of the local model under different wind loads could be obtained. As shown in Figure 6c, Y_b changed with the swing of the whole model. When the displacement of the middle part of the mid-phase jumper along the negative X direction reached the maximum, Y_b also reached the maximum ($t = 3$ s). This maximum value of Y_b (0.258 mm) was imported into the local model to obtain the stress distribution at the outlet of the tension clamp under the level-6 wind, as shown in Figure 6d. It is seen that the stress concentration appeared near the fixed end of the local model, that is, the stress concentration appeared near the outlet of the tension clamp and the maximum stress appeared here. This explains why the actual mid-phase jumper breakage occurred at the outlet of the tension clamp.

As shown in Figure 6e, with an increase in the wind load, Y_b increased, accelerating rapidly after a level-4 wind, which was due to the rapid increase in the wind load applied to the whole model. As shown in Figure 6f, with an increase in the wind load, the value of σ_a of the outermost, third, and second layers of the aluminum conductor increased, where the σ_a of the third layer was the largest. The σ_a of the outermost and third layers were higher than the yield strength of the conductor under the level-6 wind. The difference between σ_a of the outermost layer and σ_a of the third layer increased gradually with the wind load increases, and the difference was approximately 10 MPa under the level-6 wind load. As shown in Figure 6g, the steel layers had not reached their yield strength (275 MPa) when all three aluminum layers yielded under the level-7 wind load, although σ_a on the first layer was the largest at this time. This was because the Young's modulus of the first layer was much larger than that of the aluminum because of its steel material, which resulted in a larger stress on the first layer of the steel core.

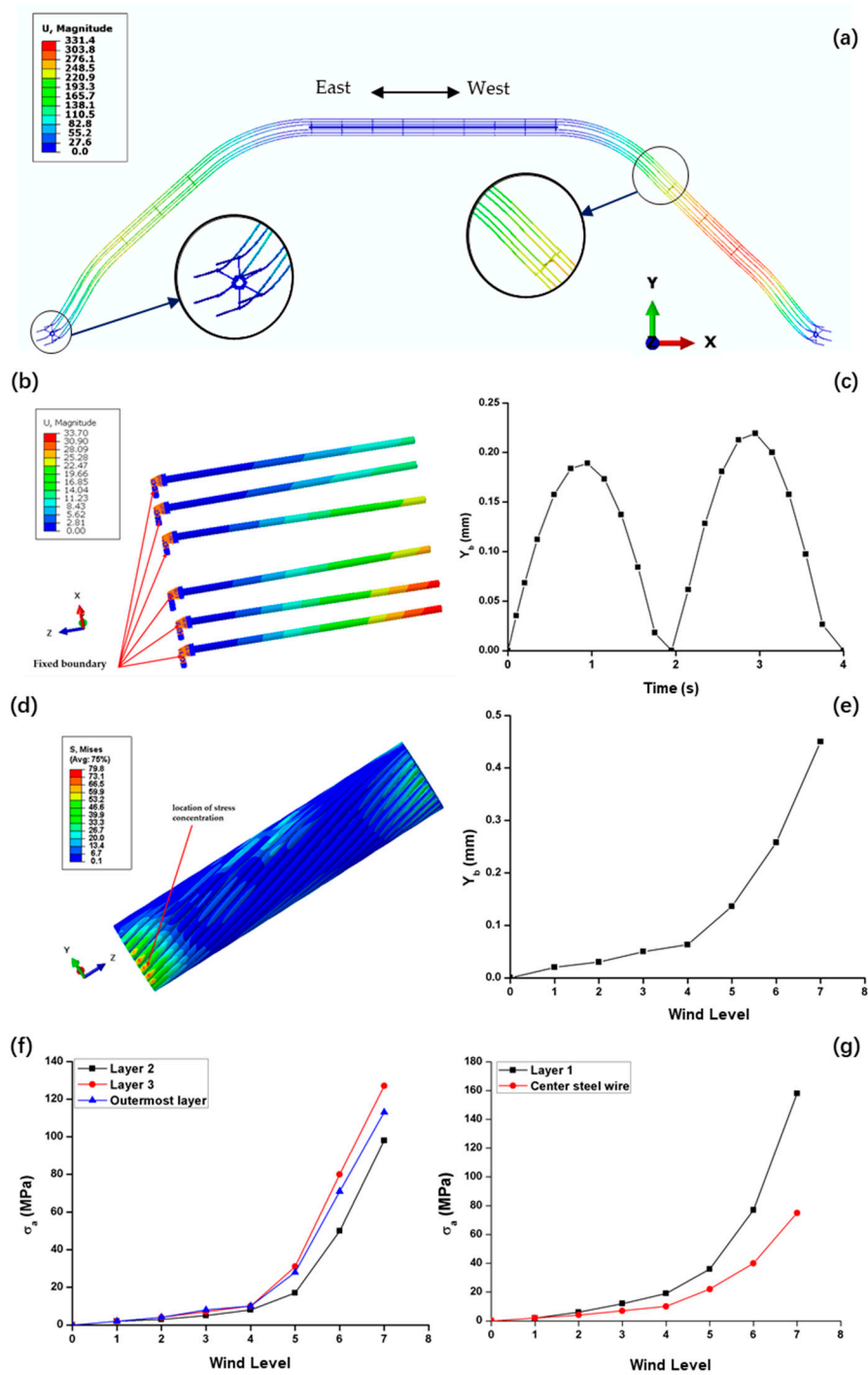


Figure 6. (a) Swing mode of the mid-phase jumper under the westerly wind, (b) the displacement nephogram of the whole model with a length of 1000 mm at the outlet of the tension clamp, (c) Y_b value of the whole model under the level-6 wind, (d) stress nephogram of the local finite element model, (e) value of Y_b corresponding to different wind loads, (f) σ_a of three aluminum conductor layers corresponding to different wind loads, and (g) σ_a of the corresponding steel layer under different wind loads.

5. Verification of Simulation Results

5.1. Verification of the Fatigue Test

Combined with the finite element simulation, the fatigue test was carried out on the fatigue test platform of an ACSR. Figure 7 shows the three-dimensional design of the fatigue test platform of an ACSR. The initial adjustment device was fixed to the tension clamp at the end of the ACSR, and the pretension and other parameters of the ACSR could be adjusted according to the working conditions on site. The axial adjustment device can exert axial tension on the ACSR. The device for transverse motion acted directly on the ACSR, causing it to move transversely, and the amplitude of the conductor swing can be adjusted. A steel-cored aluminum strand of LGJ-400/50 (Dazheng electric wire Corp, cangzhou, Hebei, China) was pressed in the tension clamp and assembled on the fatigue test platform of the ACSR. A displacement of 89 mm (Y_b) at the outlet of the tension clamp was measured using a dial indicator. The Y_b simulated by the finite element method under the level-7 wind load was set to the maximum displacement (Y_b) of 89 mm at the outlet of the tension clamp during the fatigue test, and a cyclic fatigue test was then conducted. Three groups of experiments were conducted. Table 3 shows that the cyclic fatigue life of the conductor was between 150,000 and 300,000 times without or with very little tension.

Table 3. Results of fatigue tests.

Specimen	Y_b	Cycles (Number of Times)
Specimen A	0.45	156,000
Specimen B	0.45	290,000
Specimen C	0.45	226,000

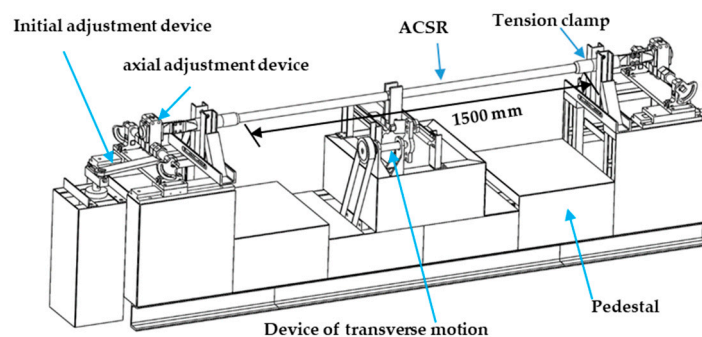


Figure 7. 3-D design drawing of the fatigue test platform of a steel-cored aluminum strand (ACSR).

As shown in Figure 8a, there was an obvious stress concentration at the outlet of the tension clamp for the outermost conductor and the third layer of conductor. As shown in Figure 8b,c, σ_a of the third layer of the conductor (79.7 MPa) was greater than σ_a of the outermost conductor (71.4 MPa), which was very interesting. Under the guidance of the finite element results, when one strand of the outermost conductor broke during the fatigue test, the outermost conductor was cut off completely, as shown by arrow A in Figure 9. Interestingly, at this time, the third layer of conductor had almost broken, as shown by arrow B in Figure 9. This indicates that at the outlet of the tension clamp, the crack of the third layer of conductor occurred earlier than the outermost conductor, which shows the accuracy of local model simulation results.

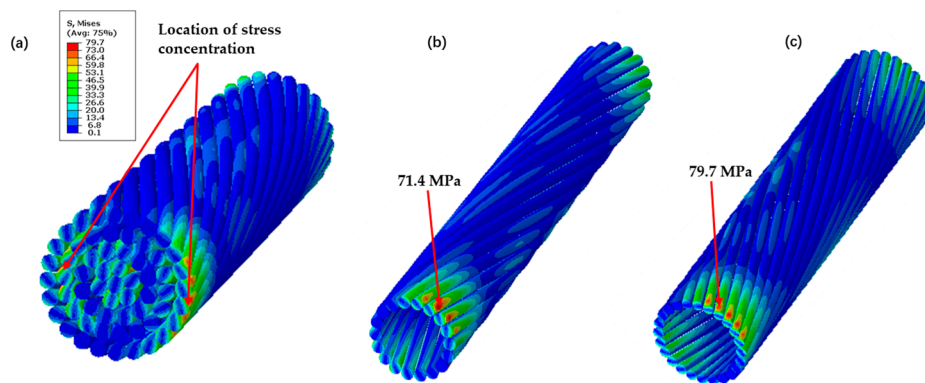


Figure 8. Stress distribution of local model at the outlet of the tension clamp: (a) the stress distribution of each layer, (b) the stress distribution of the third layer of the conductor, and (c) the stress distribution of the outmost conductor.

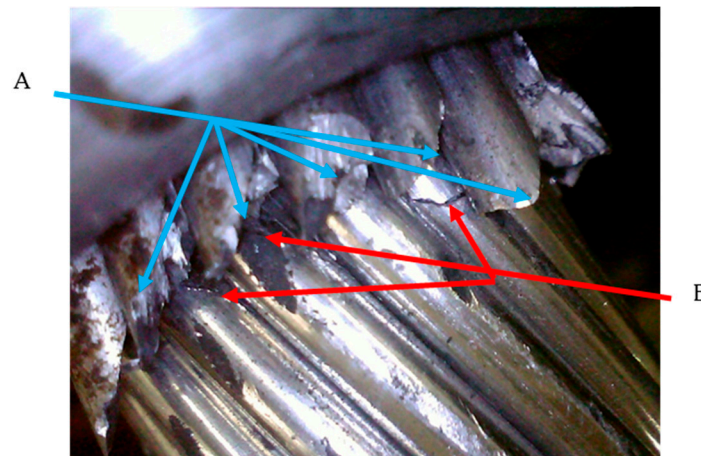


Figure 9. Fracture diagram of the third layer of conductor.

Figure 10a shows the macroscopic morphology of the fatigue fracture. As shown in Figure 10b, the fatigue band with the characteristics of bainite lines was observed. These fatigue bands were thick, short, deep, wide, and discontinuous, which obviously accorded with the characteristics of low cycle fatigue fracture bands. Therefore, under the level-7 wind load, the stress concentration of the third layer at the outlet of the tension clamp had yielded. To summarize, the results of the fatigue tests were in good agreement with the simulation results, which proved the accuracy of the local model simulation results.

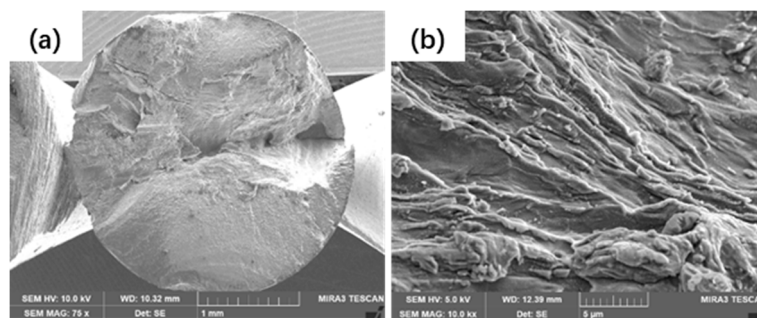


Figure 10. (a) The macroscopic morphology of the fatigue fracture, and (b) morphology of the fatigue fracture.

As shown in Figure 11a, after cutting the outermost conductor, it was found that the third layer of the conductor has obvious wear on the surface at the outlet of the tension clamp. As shown in Figure 11b, after the experiment, several wear defects could be seen on the surface of the third layer of conductor at the outlet of the tension clamp after cutting. The outer surface of the third layer led to wear defects due to the sliding of the conductor in the process of moving. These defects became the source of cracks in the third layer of conductor, and the cracks eventually continued to expand in the process of repeated cyclic movement of the conductor, resulting in the fracture of the third layer of conductor.

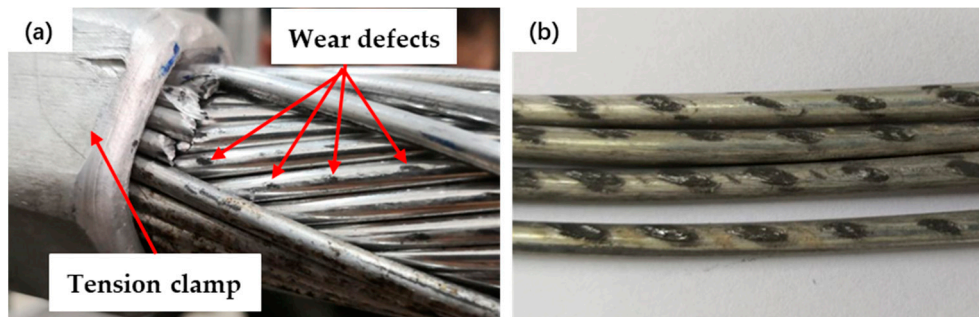


Figure 11. (a) Wear defects on the surface of the third layer of conductor, and (b) wear defects of the third layer of conductor at the outlet of the tension clamp after cutting.

5.2. Verification of the Strain Gauges Test

In order to verify the accuracy of the finite element model, strain gauges were pasted at the outlet of the clamp. When Y_b changed, σ_a was measured under different wind loads and compared with the simulated stress. Because the strain gauge needed to be pasted on a smooth surface, the surface of the single strand of aluminum wire to be pasted with the strain gauge was lightly polished with a file. The thickness of the polished part accounted for about one fifth of the diameter of the single strand. The model of static strain instrument used was YE2538A (Yutian Technology Company, Wuxi, China). The strain gauge used was a conventional small resistance strain gauge with the size of $0.5 \text{ mm} \times 0.5 \text{ mm}$ and a sensitivity of 2.00 kV . Figure 12 shows the installation position of strain gauges.

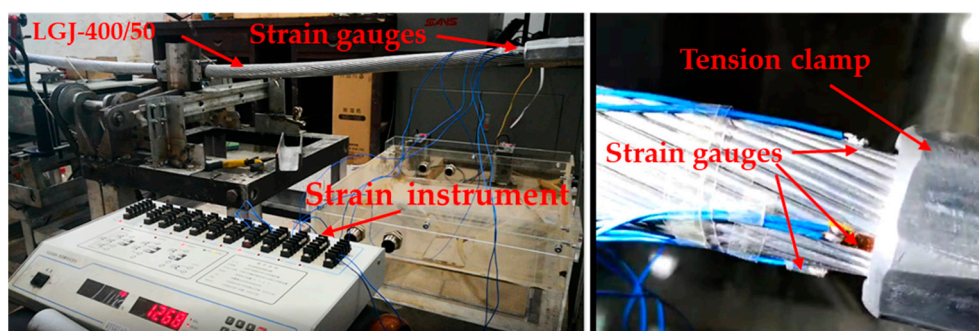


Figure 12. Installation positions of the strain gauges.

As shown in Figure 13, with the increase of the wind load, the σ_a obtained using the simulation and σ_a obtained using the test both increased, and the maximum error between σ_a obtained using the simulation and σ_a obtained using the test was about 20 MPa. On one hand, the error was the error of experimental measurement, on the other hand, it was the error of the finite element numerical calculation itself. In conclusion, although there was an error between σ_a obtained using the simulation and σ_a obtained using the test, it also proved that the accuracy of the finite element model results were within a reasonable range.

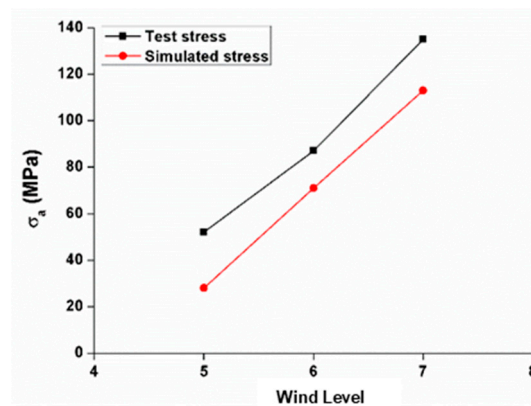


Figure 13. Comparison of the simulated stress and test stress under different wind loads.

6. Effect of the Friction Coefficient

Because the friction coefficient is affected by the metal type, chemical composition, surface state, deformation temperature, and contact pressure, the friction coefficient between aluminum strands is not easy to determine. This paper mainly studied the bending deformation of a conductor, and the contact between each strand of a conductor is extremely complex during the process of the bending deformation. Coulomb's law was introduced to study this problem. The tangential contact of each strand in the aluminum strand follows this law. The Coulomb friction model was used in Abaqus.

Papailiou et al. [25] proposed a conductor model that can withstand both the tension and bending loads, and considered the interlayer friction and slip during the process of wire bending. It was found that the bending analysis of the conductor was extremely sensitive to the selection of the friction coefficients between two adjacent layers of the conductors. The range of friction coefficients between cables was found to be between 0.55 and 0.9. Wharton et al. [26] measured the fretting fatigue strength of A1-4Mg-0.7Mn in contact with aluminum and copper. It was found that the friction coefficient of A1-4Mg-0.7Mn in contact with aluminum and copper was extremely low, but with an increase in the number of fatigue cycles, the friction coefficient increased to approximately 1.0 and remained unchanged at this value. Clearly, a conductor bending analysis is extremely sensitive to the choice of friction coefficient between two adjacent conductors. In the process of long-term service, the friction coefficient between strands of a conductor will change due to the wear between strands. In order to accurately evaluate the change of the friction coefficient in the service process of the mid-phase jumper, this section discusses the influence of the friction coefficient on the stress of the mid-phase jumper when other conditions remain unchanged. Thus, the friction coefficients between the steel-cored aluminum strands were set to 0.3, 0.5, and 0.7. At this time, the equivalent Young's modulus of the whole finite element model was 6.78, 6.68, and 7.67 GPa, respectively, and the other conditions remained unchanged. The influence of the friction coefficient is discussed next.

As shown in Figure 14, between level-1 and level-3 wind loads, the wind load was small, and thus σ_a and Y_b were extremely small; therefore, the friction coefficient had little effect on the corresponding σ_a and Y_b . Between level-4 and level-7 wind loads, when the friction coefficient was 0.115 to 0.50, σ_a and Y_b first decreased and then increased with an increase of the friction coefficient under the same wind load; when the friction coefficient was 0.50 to 0.70, σ_a and Y_b decreased again with an increase of the friction coefficient under the same wind load. Therefore, the friction coefficient had a great effect on the corresponding σ_a and Y_b between level-4 and level-7 wind loads. The difference in σ_a between the outermost layer and the third layer reached the maximum under a level-7 wind load when the friction coefficient took the above four parameters, and the maximum difference did not exceed 20 MPa. In conclusion, the friction coefficient influenced the bending of the mid-phase jumper, but the effect was not great.

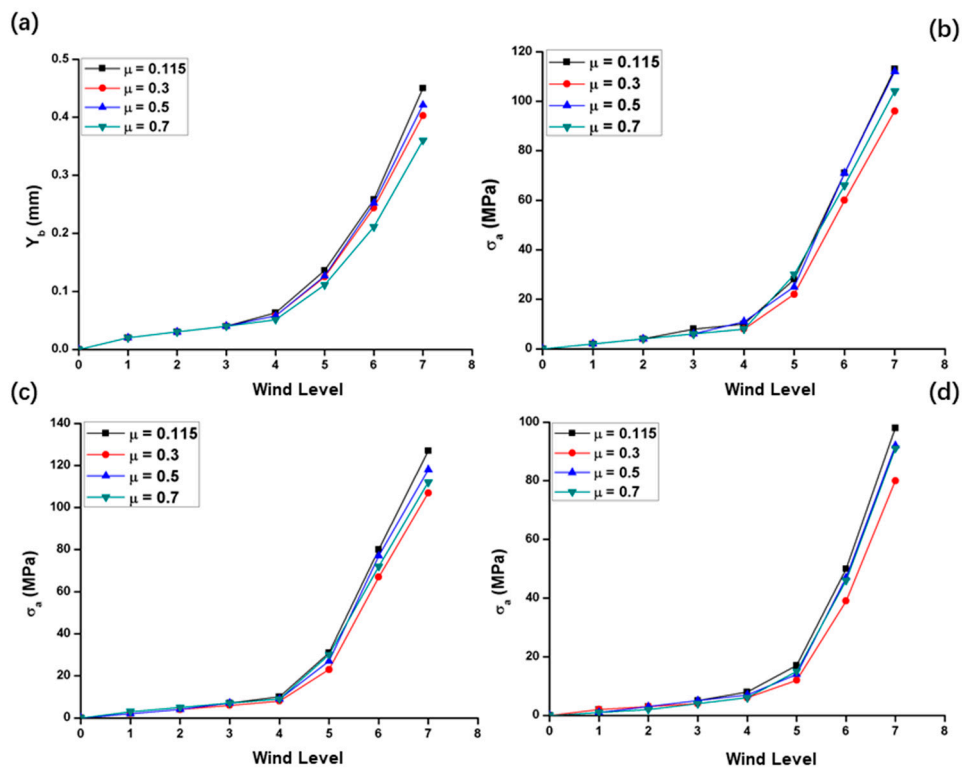


Figure 14. (a) Effect of the friction coefficient on Y_b , (b) σ_a of the outermost layer, (c) σ_a of the third layer, and (d) σ_a of the second layer.

7. Conclusions

In this paper, a finite element, fully three-dimensional solid modeling method was used to study the mechanical response of a steel-cored aluminum strand (ACSR) with a mid-phase jumper under a wind load. The whole model (simplifying an ACSR into a solid cylinder) and a local model (modeling according to the actual structure of an ACSR) of the mid-phase jumper were established. First, the movement of the mid-phase jumper of the tension tower under a wind load was studied based on a whole finite element model, and the equivalent Young’s modulus of the whole model was adjusted based on the local model. The results of the whole model were then imported into the local model, and the stress distribution of each strand of the ACSR was analyzed in detail to provide guidance for the treatment measures. Therefore, the whole model and the local model complemented each other, which could reduce the number of model operations and ensure the accuracy of the results. Although this method was applied to the stress and deformation analysis of a mid-phase jumper in this paper, it can be used to study the bending deformation of rope structures with a complex geometry and a main bending deformation.

The analysis showed that the swing of the mid-phase jumper in the east–west direction caused a greater bending moment at the lower area of the mid-phase jumper, which led to the stress concentration appearing near the outlet of the tension clamp. This explained why the actual mid-phase jumper breakage occurred at the outlet of the tension clamp. The maximum stresses of the outermost and third layers were higher than the yield strength under a level-6 wind. The difference in σ_a between the outermost and third layers increased gradually when the wind load increased, and the difference was approximately 10 MPa under a level-6 wind load.

Interestingly, σ_a of the third layer of the conductor (79.7 MPa) was greater than σ_a of the outermost conductor (71.4 MPa), which was verified by the results of the fatigue tests. Based on the analysis of the surface wear of the third layer of the conductor, the reason for the fracture of the third layer of

conductor was explained. The feasibility of the element modeling method was verified through a comparison with the results of a subsequent series of experiments.

In addition, the effects of the friction coefficient on the bending of a mid-phase jumper were studied. It was found that the friction coefficient influenced the bending of the mid-phase jumper, but the effect was not great.

Author Contributions: Methodology, W.X., P.M., and C.H.; validation, P.M. and W.X.; investigation, C.H.; data curation, P.M.; writing—original draft preparation, P.M.; writing—review and editing, W.X.; project administration, Y.L.; funding acquisition, J.H. All authors have read and agreed to the published version of the manuscript.

Funding: This work was supported by the State Grid of China Science and Technology Project, under the grant no. 52130417002U.

Conflicts of Interest: The authors declare no conflict of interest.

References

1. *Transmission Line Reference Book: "The Orange Book"*; Electric Power Research Institute: Palo Alto, CA, USA, 1979.
2. Azevedo, C.R.F.; Henriques, A.; Filho, A.R.P.; Ferreira, J.L.A. Fretting fatigue in overhead conductors: Rig design and failure analysis of a grosbeak aluminium cable steel reinforced conductor. *Eng. Fail. Anal.* **2009**, *16*, 136–151. [[CrossRef](#)]
3. Zhou, Z.R.; Cardou, A.; Fiset, M.; Goudreau, S. Fretting fatigue in electrical transmission lines. *Wear* **1994**, *173*, 179–188. [[CrossRef](#)]
4. Harvard, D.; Bellamy, G.; Buchan, P.; Ewing, H.; Horrocks, D.; Krishnasamy, S.; Motlis, J.; Yoshiki-Gravelsins, K. Aged ACSR conductors. I. Testing procedures for conductors and line items. *IEEE Trans. Power Deliv.* **1992**, *7*, 581–587. [[CrossRef](#)]
5. Chen, G.; Wang, X.; Wang, J.; Liu, J.; Zhang, T.; Tang, W. Damage investigation of the aged aluminium cable steel reinforced (ACSR) conductors in a high-voltage transmission line. *Eng. Fail. Anal.* **2012**, *19*, 13–21. [[CrossRef](#)]
6. Zhou, Z.; Cardou, A.; Goudreau, S.; Fiset, M. Fundamental investigations of electrical conductor fretting fatigue. *Tribol. Int.* **1996**, *29*, 221–232. [[CrossRef](#)]
7. Ramey, G.E.; Townsen, J.S. Effects of clamps on fatigue of ACSR conductors. *Energy Div. ASCE* **1981**, *107*, 103–119.
8. Rizzo, P.; Sorri, E.; Di Scalea, F.L.; Viola, E. Wavelet-based outlier analysis for guided wave structural monitoring: Application to multi-wire strands. *J. Sound Vib.* **2007**, *307*, 52–68. [[CrossRef](#)]
9. Castellano, A.; Foti, P.; Fraddosio, A.; Galiotti, U.; Marzano, S.; Piccioni, M.D. Characterization of Material Damage by Ultrasonic Immersion Test. *Procedia Eng.* **2015**, *109*, 395–402. [[CrossRef](#)]
10. Neslušan, M.; Bahleda, F.; Minárik, P.; Zgútová, K.; Jambor, M. Non-destructive monitoring of corrosion extent in steel rope wires via Barkhausen noise emission. *J. Magn. Magn. Mater.* **2019**, *484*, 179–187. [[CrossRef](#)]
11. Raoof, M.; Hobbs, R.E. The Bending of Spiral Strand and Armored Cables Close to Terminations. *J. Energy Resour. Technol.* **1984**, *106*, 349–355. [[CrossRef](#)]
12. Lanteigne, J. Theoretical Estimation of the Response of Helically Armored Cables to Tension, Torsion, and Bending. *J. Appl. Mech.* **1985**, *52*, 423–432. [[CrossRef](#)]
13. LeClair, R.A.; Costello, G.A. Axial, Bending and Torsional Loading of a Strand with Friction. *J. Offshore Mech. Arct. Eng.* **1988**, *110*, 38–42. [[CrossRef](#)]
14. Hong, K.-J.; Der Kiureghian, A.; Sackman, J.L. Bending Behavior of Helically Wrapped Cables. *J. Eng. Mech.* **2005**, *131*, 500–511. [[CrossRef](#)]
15. Judge, R.; Yang, Z.; Jones, S.; Beattie, G. Full 3D finite element modelling of spiral strand cables. *Constr. Build. Mater.* **2012**, *35*, 452–459. [[CrossRef](#)]
16. Zhang, D.; Ostoja-Starzewski, M. Finite Element Solutions to the Bending Stiffness of a Single-Layered Helically Wound Cable with Internal Friction. *J. Appl. Mech.* **2015**, *83*, 031003. [[CrossRef](#)]
17. Zhou, W.; Tian, H. A novel finite element model for single-layered wire strand. *J. Cent. South Univ. Technol.* **2013**, *20*, 1767–1771. [[CrossRef](#)]

18. Beleznai, R.; Páczelt, I. Design curve determination for two-layered wire rope strand using p-version finite element code. *Eng. Comput.* **2013**, *29*, 273–285. [[CrossRef](#)]
19. Lalonde, S.; Sébastien, R.; Guilbault, R.; Légeron, F. Modeling multilayered wire strands, a strategy based on 3D finite element beam-to-beam contacts—Part I: Model formulation and validation. *Int. J. Mech. Sci.* **2017**, *126*, 281–296. [[CrossRef](#)]
20. Lalonde, S.; Guilbault, R.; Langlois, S. Modeling multilayered wire strands, a strategy based on 3D finite element beam-to-beam contacts—Part II: Application to wind-induced vibration and fatigue analysis of overhead conductors. *Int. J. Mech. Sci.* **2017**, *126*, 297–307. [[CrossRef](#)]
21. Diana, G.; Belloli, M.; Giappino, S.; Manenti, A.; Mazzola, L.; Muggiasca, S.; Zuin, A. A Numerical Approach to Reproduce Subspan Oscillations and Comparison with Experimental Data. *IEEE Trans. Power Deliv.* **2014**, *29*, 1311–1317. [[CrossRef](#)]
22. Wang, J. Overhead Transmission Line Vibration and Galloping. In Proceedings of the 2008 International Conference on High Voltage Engineering and Application, Chongqing, China, 9–12 November 2008; Institute of Electrical and Electronics Engineers (IEEE): Piscataway, NJ, USA, 2008; pp. 120–123.
23. Ohkuma, T.; Kagami, J.; Nakauchi, H.; Kikuchi, T.; Takeda, K.; Marukawa, H. Numerical analysis of overhead transmission line galloping considering wind turbulence. *Electr. Eng. Jpn.* **2000**, *131*, 19–33. [[CrossRef](#)]
24. Utting, W.; Jones, N. The response of wire rope strands to axial tensile loads—Part I. Experimental results and theoretical predictions. *Int. J. Mech. Sci.* **1987**, *29*, 605–619. [[CrossRef](#)]
25. Papailiou, K. On the bending stiffness of transmission line conductors. *IEEE Trans. Power Deliv.* **1997**, *12*, 1576–1588. [[CrossRef](#)]
26. Wharton, M.; Waterhouse, R.; Hirakawa, K.; Nishioka, K. The effect of different contact materials on the fretting fatigue strength of an aluminium alloy. *Wear* **1973**, *26*, 253–260. [[CrossRef](#)]



© 2020 by the authors. Licensee MDPI, Basel, Switzerland. This article is an open access article distributed under the terms and conditions of the Creative Commons Attribution (CC BY) license (<http://creativecommons.org/licenses/by/4.0/>).